A High-Frequency Insertion Loss Enhanced Active EMI Filter With Integrated PCB Rogowski Coil CM Current Sensor

Yuan Feng, *Student Member, IEEE*, Peng Guo, *Member, IEEE*, Qianming Xu, *Member, IEEE*, Cheng Tang, Yuanfa Peng, Qiaopo Xiong, Yandong Chen, *Senior Member, IEEE*, Zhikang Shuai, *Senior Member, IEEE*, and An Luo, *Senior Member, IEEE*

***Abstract*—The wide bandgap semiconductor increases the power density of switching power supplies while bringing about serious common-mode (CM) electromagnetic interference (EMI) problems. Compared to conventional passive EMI filters (PEFs), active EMI filters (AEFs) cancel the noise by sensing and injecting, which significantly reduces the volume of the filter. However, there is a challenge in simultaneously achieving high transient voltage immunity and compact design in the sensing part. Moreover, the high-frequency insertion loss is limited largely due to stray parameters and insufficient bandwidth of active components in the injecting part. To overcome these challenges, this article presents three key contributions: First, a novel Rogowski coil CM current sensor with lead compensation is proposed. The multivariate function of mutual inductance of the coil is derived and used to reduce the size of sensor while maintaining high sensitivity and high transient voltage immunity. Second, a high-order lead compensation network is adopted to counteract the phase lag of active components at high frequencies. Third, the degradations of the injecting part caused by stray parameters are analyzed, and a high-frequency insertion loss enhanced injecting circuit is proposed to mitigate the degradation by closed-loop variable gain control. The effectiveness of the proposed AEF has been verified on a 3-kW inverter experimental platform. With a small size of 38 mm × 23 mm, the proposed AEF achieves an insertion loss of 22.8 dB–30.3 dB at high frequencies (10 MHz–30 MHz) and a maximum of 44.7 dB at 1.4 MHz.**

***Index Terms*—Active EMI filter (AEF), common-mode noise, electromagnetic interference (EMI), high-frequency, insertion loss, Rogowski coil sensor.**

Received 10 June 2025; revised 18 September 2025; accepted 18 October 2025. Date of publication 27 October 2025; date of current version 19 January 2026. This work was supported in part by the National Natural Science Foundation of China under Grant 52577191, Grant 52177178, Grant 52207198, and Grant 52127901, in part by the National Science and Technology Major Project; in part by the Natural Science Foundation of Hunan Province under Grant 2024JJ5077, and in part by the Fundamental Research Funds for the Central Universities. Recommended for publication by Associate Editor F. Costa. *(Corresponding author: Peng Guo.)*

Yuan Feng, Peng Guo, Qianming Xu, Cheng Tang, Yuanfa Peng, Yandong Chen, Zhikang Shuai, and An Luo are with the State Key Laboratory of High-Efficiency and High Quality Conversion for Electric Power, Hunan University, Changsha 410082, China (e-mail: fengyuan@hnu.edu.cn; pengguo92@hnu.edu.cn; xqm@hnu.edu.cn; tc_byron@hnu.edu.cn; hnu.pyf.cn@hnu.edu.cn; yandong_chen@hnu.edu.cn; szk@hnu.edu.cn; an_luo@hnu.edu.cn).

Qiaopo Xiong is with the Hubei Provincial Key Laboratory of Low Frequency Electromagnetic Communication Technology, WMCRI, Wuhan 430000, China (e-mail: 403864117@qq.com).

Color versions of one or more figures in this article are available at https://doi.org/10.1109/TPEL.2025.3625581.

Digital Object Identifier 10.1109/TPEL.2025.3625581

I. Introduction

THE application of wide bandgap semiconductor power devices has significantly improved the performance of digital power amplifiers. However, the high frequency and high voltage switching action also bring electromagnetic interference (EMI) problems [1]. To meet electromagnetic compatibility (EMC) standards, passive EMI filters (PEFs) are widely used because of low cost and high stability [2], but they require large common-mode (CM) inductors due to the limitation of leakage current. Active EMI filters (AEFs) detect current or voltage noise and then inject a compensating voltage or current opposite to the noise through an active circuit [3]. In this way, the size of the CM inductor can be reduced while maintaining high insertion loss [4]. AEFs usually consist of two parts: 1) sensing part; and 2) injecting part.

According to type of sensing part, AEFs can be categorized into voltage sensing AEFs and current sensing AEFs. Voltage sensing AEFs only use resistor and capacitor (RC) networks to sense the CM voltage, which have the advantage of small size [5], [6], [7], but it is susceptible to high transient voltages [8]. Another disadvantage lies in the requirement to design a stabilization network specifically adapted to the characteristics of the filter and its operating environment [9]. Current sensing AEFs usually use current transformers (CTs) to sense CM currents [9], [10], so high transient voltage immunity is achieved, but the use of magnetic cores increases the size. In addition, the magnetic permeability decreases with increasing frequency [12], and excessive CM currents can lead to magnetic saturation, which can result in nonlinearities in the sensing gain for CM currents. Ferrite cores are noted to be the preferred choice for sensing high-frequency currents, but high performance cores rise the cost [13]. In contrast with CTs, the printed circuit board (PCB) Rogowski coil is a hollow transformer, which has a small size and high linearity, but also results in a lower gain than the CT [14]. Therefore, Rogowski coil can serve as a high-frequency current sensor, which has been applied in a ripple filter on the output of a buck converter [15]. However, due to the low sensitivity of Rogowski coils, the CT sensor is still more advantageous for low-current (<20A) systems. As a result, Rogowski coils are more commonly used to measure

TABLE I
COMPARISON OF THE PROPOSED AEF AND EXISTING AEFS/HEFS

AEF	Sensing type	HTV immunity	Size /mm	IL/dB	Effective f range /MHz	Additional L_{CM} /mH	Main cost components (including CM chokes)	Cost
TI [5]	RC	+	28*19	15-30	0.15-3	1+4	1*OP, 2*CM chocks	++
Li et al. [6]	RC	+	30*25	20-30	0.15-3	0.5	2*OPs, 2*BJTs, 1*CM chock	+++
Chen et al. [7]	RC	+	29*17	10-24	0.15-10	0.23	1*OP, 2*BJTs, 1*CM chock	+++
Shin et al. [9]	CT	+++	53*53	5-25	0.15-6	1+8	1*CT, 2*BJTs, 2*CM chocks	++
Li et al. [10]	CT	+++	60*50	21-46	0.15-30	-	1*CT, 1*OP, 2*BJTs	+
The proposed AEF	RCCS	++	38*23	23-47	0.15-30	-	2*OPs, 2*BJTs	++

CT=current transformer, RC=resistor and capacitor, RCCS =Rogowski coil sensor, HTV=High transient voltage immunity, IL=Insertion loss, OP=Operational amplifier, Effective f range=Effective frequency range, L_{CM} = common-mode inductance

high frequency and large currents such as switching currents and pulsed currents [16], [17]

Similarly, for the injecting part, AEFs can be categorized into voltage injecting AEFs and current injecting AEFs. For voltage injecting AEFs, a transformer is needed to inject the opposite voltage [18], which tends to be large in size and of limited high-frequency characteristics. For the current injecting AEFs, the oppsite current is injected via a capacitive branch, which is more convenient than the voltage injecting AEF, so it is widely used in commercial ac/dc converter [19], motor drive system [20] and grid-connected inverter [21]. However, the gain (from measured CM current/voltage to injected current) tends to deviate from the desired value, especially at high frequencies. The error of gain finally leads to dissatisfied insertion loss. A virtual impedance analysis method is proposed [22], which shows that the gain should not be constant but equal to the impedance of the injection branch. Further, to fulfill the gain requirement at high frequencies, the stray inductance of the capacitor in the injecting branch should also be considered [23]. Nevertheless, stray parameters such as the variable output resistance of the operational amplifier, stray inductance in the ground lead, etc., also lead to insertion loss decreases at high frequencies. What is worse, even if the stray parameters of the injection branch can be fully accounted for, the insertion loss still degrades due to the limited bandwidth of active components, such as operational amplifiers (op-amps) and transistors. It is pointed out that the phase lag caused by op-amps may even lead to the noise being amplified at high frequencies [24]. Therefore, because of the insufficient high-frequency performance, it is difficult for AEFs to maintain high insertion loss at 150 kHz–30 MHz to meet the EMI standard (such as CISRP-11) without adding passive components. The parameters of the two most popular types (current-sensing-current-injecting and voltage-sensing-current-injecting) of AEFs are compared in Table I.

Aiming to above problems in the sensing part and the injecting part, the main contributions of this article are as follows:

1) A novel Rogowski coil CM current sensor is proposed. The multivariate function of mutual inductance of the coil is derived to reduce the size of sensor compared to CTs while maintaining high transient voltage immunity compared to RC networks.
2) A high-order lead compensation network (LCN) optimized by evolution algorithms is proposed. The network counteracts the phase lag of active components and thus improves insertion loss at high frequencies.
3) A high-frequency insertion loss enhanced injection circuit is proposed. The degradations of the injecting part caused by stray parameters are analyzed and mitigated by closed-loop variable gain control (VGC). Finally, the insertion loss at high frequencies is furtherly improved.

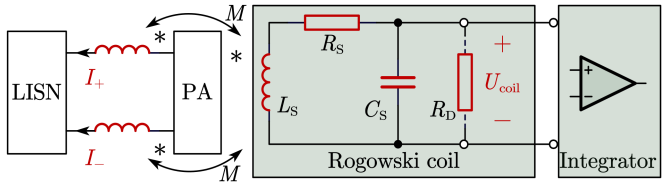

Fig. 1 Schematic diagram of the Rogowski CM current sensor.

These three contributions enable the insertion loss of the proposed AEF to reach 22.8 dB–30.3 dB at high frequencies (10 MHz–30 MHz) and a maximum of 44.7 dB at 1.4 MHz, with a small size of 38 mm∗23 mm.

The rest of this article is organized as follows. In Section II, the principle and design of the novel Rogowski coil CM current sensor with high-order lead compensation network are presented. In Section III, the high-frequency insertion loss enhanced injection circuit is introduced. In Section IV, an experimental platform with a 3 kW inverter is built to verify the proposed method. Finally, Section V concludes this article.

II. DESIGN OF THE ROGOWSKI CM CURRENT SENSOR WITH LEAD COMPENSATION

A. Modeling and Structure Optimization of Rogowski Coil

The equivalent circuit diagram of the CM current sensor based on the Rogowski coil is shown in Fig. 1, and the structure of the Rogowski coil is shown in Fig. 2. The coil is a uniformly wound closed circular coil. Compared with split-core Rogowski coils [25] or rectangular Rogowski coils [26], the closed circular Rogowski coil offers the best geometrical symmetry to maintain immunity to external magnetic fields in a complex electromagnetic environment.

Meanwhile, due to the symmetry, the magnetic flux of the differential-mode current is cancelled out in the coil, while the CM current generates the same induced voltage. In Fig. 1,

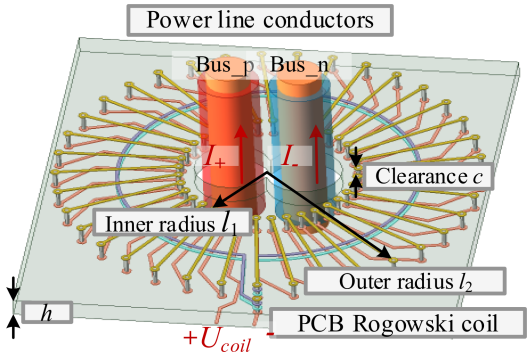

Fig. 2 Structure of the Rogowski coil for CM current sensing.

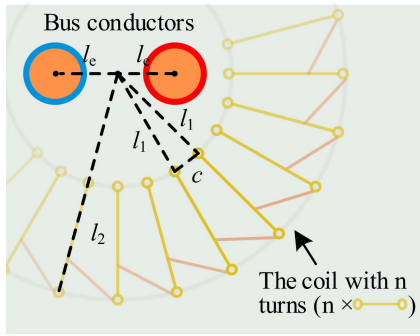

Fig. 3 Top view of the relative position between the power line conductors and the coil.

M represents the mutual inductance between the coil and two power bus conductors of the noise source, and L_S represents the self-inductance of the coil. R_S is the resistance of the coil winding, usually only a few ohms, and C_S is the stray capacitance of the coil, generally at picofarad level. Since the value of R_S is relatively small and can generally be ignored, the resonant frequency of the Rogowski coil can be expressed as:

$$f_{\text{res}} = 1/(2\pi\sqrt{L_s C_s}) \tag{1}$$

When the signal frequency f is much lower than the resonant frequency, the coil can be approximately regarded as a differentiator, whose output voltage can be expressed as

$$U_{\text{coil}}(t) = M\frac{di_{cm}(t)}{dt}(f \ll f_{\text{res}}). \tag{2}$$

Then, U_{coil} is integrated through the integrator to reproduce the CM current. Ideally, the output of the integrator is

$$U_{\text{int}}(t) = \int U_{\text{coil}}(t)dt = KMi_{cm}(t)(f \ll f_{\text{res}}). \tag{3}$$

Without a magnetic core, the value of M is generally very small. Moreover, the bandwidth of the integrator is limited, so the gain factor K cannot be too large. Therefore, the design of the Rogowski coil should achieve the following two goals.

1) f_{res} should significantly exceed the concerned frequency.
2) M should be as large as possible.

When the winding is dense enough, the voltage error caused by the eccentricity of the conductor can be ignored [27]. Therefore, the power bus can be regarded as conductors passing through the center of the coil. Since the lengths of the conductors are much greater than the thickness of the coil, they can be regarded to be infinitely long. According to Biot-Savart's law, the magnetic flux density B near the conductors can be expressed as

$$B = \frac{\mu_0 I}{2\pi r} \tag{4}$$

where μ_0, I, and r are the vacuum permeability, the current of the conductor, and the distance between the analyzed point and the center of the conductor, respectively.

Assuming that the coil is composed of n turns of uniform windings, the total magnetic flux linkage in the coil can be expressed as

$$\psi(t) = n\oiint_s Bds = n\int_{l_1}^{l_2}\frac{\mu_0 i_{cm}(t)}{2\pi r}hdr = \frac{\mu_0 nhi_{cm}(t)}{2\pi}\ln\frac{l_2}{l_1} \tag{5}$$

where l_1 is the inner radius, l_2 is the outer radius, n is the number of turns, and h is the height of the coil as shown in Fig. 2. The mutual inductance M and induced voltage u_{ind} of the coil can be expressed as

$$M(l_1, l_2, n, h) = \frac{\psi(t)}{i_{cm}(t)} = \frac{\mu_0 nh}{2\pi}\ln\frac{l_2}{l_1} \tag{6}$$

$$u_{\text{ind}}(t) = \frac{d\psi}{dt} = M\frac{di}{dt} = \frac{\mu_0 nh}{2\pi}\ln\frac{l_2}{l_1}\frac{di}{dt}. \tag{7}$$

As it can be seen in Fig. 3, the number of turns n is equal to the number of vias in the inner layer of the coil. Due to PCB manufacturing limitations, the via clearance (noted as c) cannot be too small. The number of turns n and the inner radius l_1 are negatively correlated, specifically

$$n_{\max}(c, l_1) = \pi/\arcsin[c/(2l_1)] \tag{8}$$

where $c_{\min}<c<l_1$ and n is an integer. According to (7) and (8), M can be further derived as

$$M(l_1, l_2, c, h) = \frac{\mu_0 h}{2\arcsin(\frac{c}{2l_1})}\ln\frac{l_2}{l_1}. \tag{9}$$

It can be seen from (9) that when the coil structure parameters are determined, the induced voltage of the coil is proportional to the differential of the measured current. While CTs must consider the variation of the magnetic permeability of the coil core with frequency and the saturation effect. To recover the phase of the CM current, an integrator is required. Without considering the influence of the stray parameters of the Rogowski coil, the gain of the integrating circuit should be

$$G_{\text{int}}(s) = \frac{G_{cm}}{u_{\text{ind}}/I(s)} = \frac{G_{cm}}{sM} \tag{10}$$

where G_{cm} is the desired output sensitivity of the CM current sensor. Since the integrator is generally composed of voltage feedback operational amplifiers, the gain bandwidth product (GBW) is generally limited. The required GBW of the integrator

GBW_{int} is obtained

$$GBW_{\text{int}} = |G_{\text{int}}(s)|_{s=j\times 2\pi f}| \times f = \frac{G_{cm}}{2\pi M}. \tag{11}$$

Excessive requirement for the GBW will lead to the increase in the cost of op-amp chips, the decrease in the signal-to-noise ratio, and even stability issues.

Unlike measuring switching current [28] or current of power modules [29], the amplitude of CM current is small (lower than 1A even in motor drive systems with large CM currents [20], [30]). Therefore, the sensor needs a high gain, which is set to be 1 V/A in the proposed sensor. In order to satisfy such a high gain of the sensor while realizing a high signal-to-noise ratio, high bandwidth and immunity to the influence of stray parameters, the mutual inductance of the Rogowski coil should be increased and thus the integrator gain can be reduced.

Therefore, it is necessary to optimize the structure of the coil to make the mutual inductance M as large as possible.

Meanwhile, excessive thickness and insufficient turn spacing will increase the cost of PCB manufacturing.

Therefore, to simplify the analysis without losing generality, it is assumed that $h = 1.6$ mm and $c_{\min} = 0.6$ mm.

From (9), it can be seen that l_1 is the key variable in the optimization of mutual inductance. A change in l_1 affects both the maximum number of turns and cross-sectional area per turn, which in turn affects the mutual inductance. Therefore, the effect of l_1 on mutual inductance should be quantitatively analyzed. Also, the relationship between M and l_2 should be derived to calculate the maximum mutual inductance at different sizes.

Since the inner l_1 and outer diameters l_2 are independent of each other, to analyze the variation of M with l_1 and l_2, the partial derivatives of M with respect to l_1 and l_2 are, respectively, obtained

$$\frac{\partial M}{\partial l_1} = \frac{u_0 h \ln\left(\frac{l_2}{l_1}\right) c}{2\arcsin\left(\frac{c}{2l_1}\right)^2 l_1^2 \sqrt{-\frac{c^2}{l_1^2}+4}} - \frac{u_0 h}{2\arcsin\left(\frac{c}{2l_1}\right) l_1} \tag{12}$$

$$\frac{\partial M}{\partial l_2} = \frac{u_0 h}{2\arcsin\left(\frac{c}{2l_1}\right) l_2}. \tag{13}$$

On the one hand, it is assumed that the coils are dense enough, namely $c \ll l_1$. Then, setting (12) equal to zero yields

$$\frac{u_0 h \ln\left(\frac{l_2}{l_1}\right)}{c} - \frac{u_0 h}{c} = 0 \tag{14}$$

namely

$$l_2 = e \cdot l_1 \tag{15}$$

where e represents the natural constant.

On the other hand, $\partial M/\partial l_2$ is monotonically decreasing and always greater than 0.

Through the above analysis of $\partial M/\partial l_1$ and $\partial M/\partial l_2$, the following two conclusions can be drawn.

1) To maximize mutual inductance as much as possible, the inner diameter l_1 should be at least greater than l_2/e.

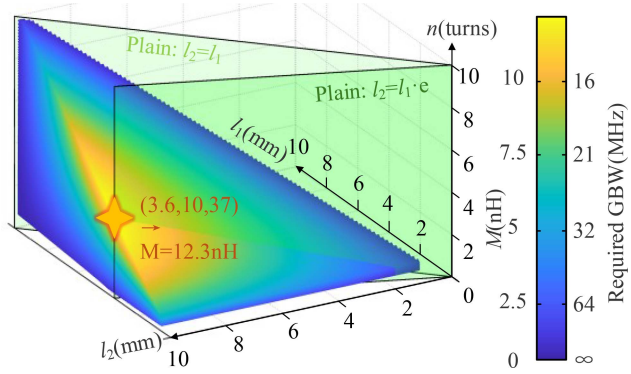

Fig. 4 Relationship between mutual inductance M, n, l_1 and l_2.

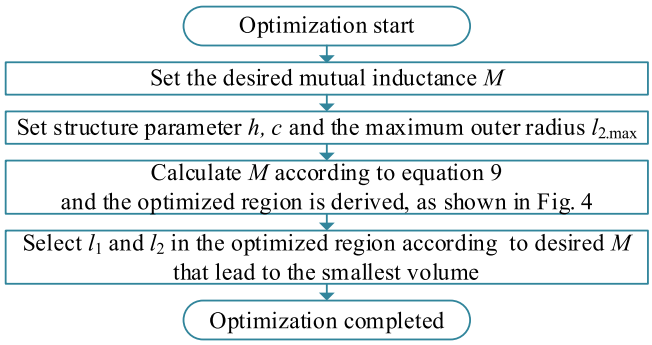

Fig. 5 Flowchart of the Rogowski coil structure optimization.

2) To reduce the size of the AEF sensing part, and decrease the trace length so that increasing the resonant frequency of the coil, an overly large outer diameter l_2 is unnecessary.

From Fig. 4, it can be seen that when l_1 is small, increasing l_1 is able to achieve a greater mutual inductance, but when l_1 exceeds l_2/e the situation is the opposite. With $N = 37$, $l_1 = 3.6$ mm and $l_2 = 10$ mm, M can be optimized to 12.3 nH. The flowchart of the optimization algorithm is shown in Fig. 5. It is worth mentioning that the tolerance of PCB height has the maximum influence on the mutual inductance ($\pm 10\%$), while the other parameters have far less influence. However, 10% can be easily compensated by adjusting the gain of the integrator. Besides, the tolerance has little influence on the bandwidth.

Assuming that the sensitivity $G_{\text{cm}} = 1$V/A, the required GBW is 13 MHz, which can be realized easily. It should be noted that although the bus conductors do not actually pass through the center of the coil, the error is negligible. The eccentricity error can be calculated as

$$\varepsilon_e(N, k_e, k_r) = \frac{1}{2N\ln k_r}\sum_{i=1}^{N}\ln\frac{1+\left(\frac{k_e}{k_r}\right)^2 - 2\left(\frac{k_e}{k_r}\right)\cos\left(i\frac{2\pi}{N}\right)}{1+k_e{}^2 - 2k_e\cos\left(i\frac{2\pi}{N}\right)} \tag{16}$$

where N is the number of turns, k_{r} is the ratio of inner radius and outer radius (namely l_2/l_1 Fig. 3), k_{e} is the eccentricity ratio (namely l_{e}/l_1 in Fig. 3). If the eccentricity error is required to be less than 0.5%, namely

$$\varepsilon_e(37, k_e, 2.78) < 0.5\%. \tag{17}$$

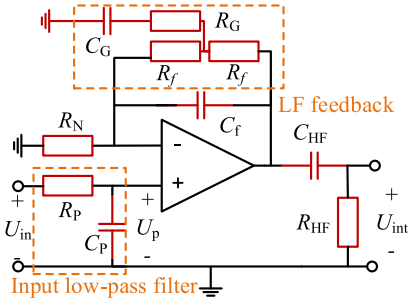

Fig. 6. Integrator in the Rogowski CM current sensor.

Solving for k_e yields that:$k_e < 0.95$. That is, when the eccentricity is <0.95, the error of the induced voltage will be less than 0.5%. Therefore, even if the conductor is very close to the edge of the coil's center hole, the error due to eccentricity can still be ignored.

B. Design of the Integrator

For the integrator used in the sensing part of the AEF, the following functions should be implemented.

1) The high-pass filtering function. Ideally, the transfer function of an integrator is K/s, where K is the gain factor. The integration gain increases as the frequency decreases, so the low-frequency (LF) noise without the concerned frequencies may cause saturation problems.
2) Sufficient phase accuracy at concerned frequencies (ideally–90°). Unlike sensors for overcurrent protection and spectrum analysis, the noise suppressing effect of the AEF is highly sensitive to phase accuracy.

For requirement 1, it can be satisfied by designing a high-pass filter. For requirement 2, when the product of signal gain and frequency is much lower than the GBW of the op-amp (namely, the op-amp is assumed to be ideal), and then the requirement can be satisfied by a reasonable design of the integration parameters. Otherwise, compensation circuits need to be designed to counteract the high-frequency phase lag of the op-amp. In fact, the phase lag is also caused by other active components such as transistors, and will also lead to insertion loss degradation. The phase lag needs to be measured before compensating. Therefore, this subsection focuses on the original integrator (without compensation). Detailed compensating method will be introduced in Section III-C.

The hybrid integrator is adopted to process the output of the Rogowski coil [31], [32], as shown in Fig. 6. With $R_p = R_N$ and $C_p = C_f$, the integrator has the best circuit symmetry, practical benefits and a simpler transfer function, which improves robustness and performance in practical applications. R_p and C_p not only form an input low-pass filter buffering the surge current in CM noise, but also form a passive integrator. The op-amp and R_N and C_f form an active integrator. The LF feedback part consists of R_f, R_G and C_G, which suppress the LF gain without affecting the high-frequency (HF) performance. The detailed working principle is as follows:

To simplify the analysis, $R_p = R_n$, $C_p = C_f$, $R_G \ll R_f$ and $R_N \ll R_f$ are usually taken. Then, it is assumed that the bandwidth

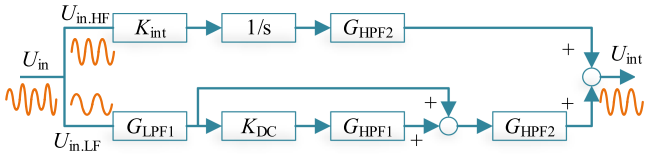

Fig. 7. Function block of the integrator.

of the op-amp is sufficient (i.e., the "virtual short" feature holds). The circuit can be divided into two modalities: LF modality and HF modality. The corner frequency between the two modalities f_C is

$$f_c = 1/(2\pi R_f C_f). \tag{18}$$

For HF signals ($f \gg f_C$), it is held that $1/(sC_f) \ll R_f$, so the LF feedback part (R_f, R_G and C_G) is bypassed. The HF output $U_{int\cdot HF}$ of the integrator can be expressed as

$$\begin{aligned} U_{int.HF} &= \frac{1}{R_p C_p s + 1} \frac{R_f C_f s}{R_f C_f s} \frac{R_{HF} C_{HF} s}{R_{HF} C_{HF} s + 1} \\ &= \frac{1}{R_N C_f s} \frac{R_{HF} C_{HF} s}{R_{HF} C_{HF} s + 1}. \end{aligned} \tag{19}$$

For LF signals ($f \ll f_C$), it is held that $1/(sC_f) \gg R_f$, so the feedback capacitor C_f is bypassed. The LF output $U_{int\cdot LF}$ of the integrator can be expressed as

$$\begin{aligned} U_{int.LF} = &\frac{1}{R_N C_f s + 1} \left[\left(1 + \frac{R_f}{R_N} \right) \left(\frac{R_f C_G s}{R_G C_G s + 1} + 2 \right) \right] \\ &\times \frac{R_{HF} C_{HF} s}{R_{HF} C_{HF} s + 1} U_{in}. \end{aligned} \tag{20}$$

According to (19) and (20), the function block of the original integrator is shown as Fig. 7, where

$$\begin{cases} K_{int} = 1/(R_N C_f) \\ K_{DC} = 1 + R_f/R_N \\ G_{LPF1} = 1/(R_N C_f s + 1) \\ G_{HPF1} = \frac{C_G s}{C_G s + 1} \\ G_{HPF2} = \frac{R_{HF} C_{HF} s}{R_{HF} C_{HF} s + 1} \end{cases}. \tag{21}$$

From the above analysis, for HF signals, the integrator is equivalent to the cascade of an integral part and a high-pass filter. For LF signals, due to $R_N \ll R_f$, the integrator is approximately equivalent to the cascade of a first-order low-pass filter and a second-order high-pass filter, ensuring that the LF gain will not be too large.

The design steps of the proposed integrator are as follows:

1) Set f_c according to the concerned frequency.
2) Set the integral gain factor K_{int} according to the required sensing sensitivity G_{cm} and mutual inductance M of the coil.
3) Set the K_{DC} according to the required LF attenuation.
4) Solve R_f R_N and C_f based on parameters set in steps 1–3. If $R_N \ll R_f$ is not satisfied, K_{DC} needs to be adjusted.
5) According to the noise frequency band of concern, set R_G, C_G, R_{HF} and C_{HF}, thereby setting the corner frequencies of the two high-pass filters.

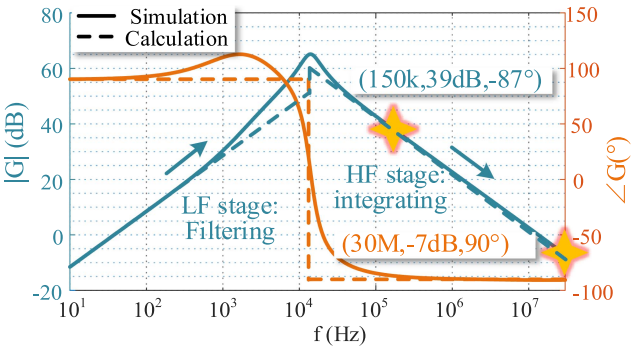

Fig. 8 Bode diagram of the integrator.

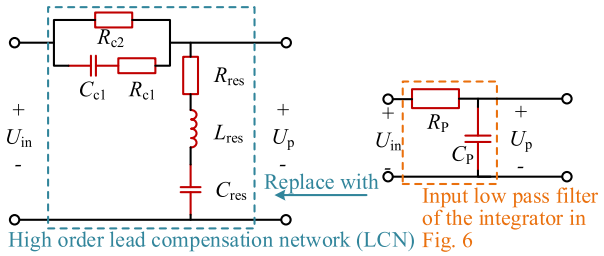

Fig. 9. Schematic diagram and connection of the high-order lead compensating network (LCN).

Assuming that the sensitivity $G_{\rm cm} = 1$V/A, the integrator is designed based on the above method. As shown in Fig. 8, the calculation result is consistent with the simulation result except that near the corner frequency. However, this does not affect the integration function at 150 kHz–30 MHz and the ability of LF noise suppression.

C. High-Order Lead Compensation Network

As shown in Fig. 9, by simply replacing the input low-pass filter in the integrator with the high-order lead compensating network (LCN), the phase lag caused by the limited bandwidth of the active components (such as op-amp and BJT) can be compensated. The proposed LCN consists of an L-C-R resonance suppression branch and an R-C-R lead compensation branch.

The basic principle of implementing compensation is to compensate for the gain of the total AEF (noted as $G_{\rm AEF}$) at high frequencies by increasing the noninverting input of op-amp $U_{\rm p}$, thus there is the following proportionality:

$$\frac{G_{\rm p.ideal}}{G_{\rm p.act}} = \frac{G_{\rm AEF.ideal}}{G_{\rm AEF.act}} \tag{22}$$

where the suffix "ideal" denotes ideal gain, "act" denotes actual gain. To maximize the insertion loss of AEF, $G_{\rm AEF}$ should be as close as possible to the injecting impedance $Z_{\rm inj}$ [22]. Combining the definitions of $G_{\rm p}$ and $G_{\rm AEF}$, there are

$$\begin{cases} G_{\rm AEF.ideal} = Z_{\rm inj} \\ G_{\rm AEF.act} = U_{\rm out.act}/I_{cm} \\ G_{\rm p.act} = U_{\rm p.act}/I_{cm} \end{cases}. \tag{23}$$

Substituting (22) into (23) gives

$$G_{\rm p.ideal} = G_{\rm p.act}\frac{G_{\rm AEF.ideal}}{G_{\rm AEF.act}} = Z_{\rm inj}\frac{U_{\rm p.act}}{U_{\rm out.act}} \tag{24}$$

where $U_{\rm out}$ is the output voltage of the AEF. Due to the complexity of the transfer function of the LCN, it is hard to fit the desired gain by theoretical calculations. Therefore, an evolutionary algorithm based on electric charged particles optimization (ECPO) method is adopted [33], and the steps are as follows:

First, $Z_{\rm inj}$, $U_{\rm p.act}$, and $U_{\rm out.act}$ are measured, and the ideal gain of $G_{\rm p.ideal}$ is calculated by (24). To calculate the gain of the Rogowski coil to the CM current, it is necessary to measure the stray parameters $R_{\rm s}$, $L_{\rm s}$, $C_{\rm s}$ and mutual inductance M of the Rogowski coil (shown in Fig. 1). The noninverting input of the op-amp $G_{\rm p}$ calculated by the algorithm is noted as $G_{\rm p.calc}$

Second, the optimization objective is set as the maximum error between $G_{\rm p.calc}$ and $G_{\rm p.ideal}$ within the concerned frequencies, which is noted as $G_{\rm p.err.max}$. The goal of the algorithm is to make $G_{\rm p.err.max}$ as small as possible on condition that the component values are of reasonable ranges. That is, the following optimization problem needs to be solved:

$$\begin{aligned} &\min |G_{\rm p.calc}(f) - G_{\rm p.ideal}(f)|_{\max} \\ &\quad stX_{i.\min} \le X_i \le X_{i.\max} \quad (i = 1..6) \end{aligned} \tag{25}$$

where $X_{\rm i}$ denotes the ith component in the LCN shown in Fig. 9, and $X_{\rm i.min}$ and $X_{\rm i.max}$ denote the lower and upper bounds on the value of that component.

Then, to accelerate the convergence, the initial value of the element can be set as follows: on the one hand, to keep the integral gain $K_{\rm int}$ consistent, $R_{\rm c2}$ and $C_{\rm res}$ can be set equal to $R_{\rm p}$ and $C_{\rm p,}$ respectively. On the other hand, to suppress the effect of the coil resonance, the value of $L_{\rm res}$ can be calculated based on the coil resonance frequency $f_{\rm res}$ initially. That is

$$\begin{cases} R_{\rm c2.init} = R_p \\ C_{\rm res.init} = C_p \\ L_{\rm res.init} = (1/2\pi f_{\rm res})^2/C_{\rm res} \end{cases} \tag{26}$$

where the suffix "init" denotes initial value, the ECPO algorithm is used to optimize the network component values so that $G_{\rm p.calc}$ is close to $G_{\rm p.ideal}$. The flowchart of the optimization algorithm is shown in Fig. 10, which can also be concluded by the following three simple steps.

1) Measure injecting impedance $Z_{\rm inj}$, the noninverting input of the op-amp $U_{\rm p.act}$ and the output of the injecting circuit $U_{\rm out.act}$. without using LCN.
2) Calculate the improved $U_{\rm p}$ to achieving lead compensation, namely $U_{\rm p.ideal}$.
3) Optimizing the LCN parameters by evolution algorithms, then $G_{\rm p}$ converges to $G_{\rm p.ideal}$.

In addition, compared to existing methods, the LCN only introduces additional passive components, so the cost has little increase. Since $G_{\rm p.ideal}$ depends heavily on the stray parameters of the coil and the zero-pole characteristics of the active components, it is difficult for the simulation to predict the experimental results. Therefore, the experimental data are used for verification, which is shown in Section IV.

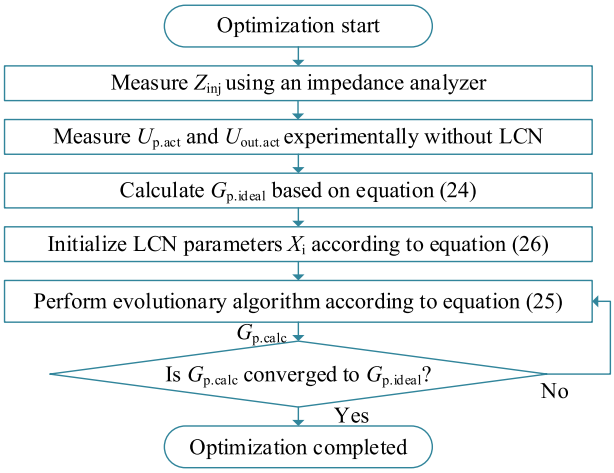

Fig. 10 Flowchart of the LCN parameter optimization.

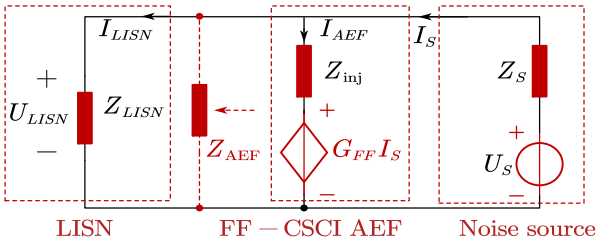

Fig. 11 CM equivalent circuit of the FF-CSCI AEF.

III. Design of the High-Frequency Insertion Loss Enhanced Injecting Circuit

A. Equivalent Circuit of the Injecting Circuit

The injection circuit is cascaded after the sensing circuit, serving as a low impedance branch to pass by the noise. For the feedback current-sensing-current-injecting (FB-CSCI) type AEF, the insertion loss is always positively correlated with the total loop gain of the AEF, but an excessively large loop gain can also bring stability issues; while for the feedforward current-sensing-current-injecting (FF-CSCI) type AEF, the maximum insertion loss is reached when the loop gain equals to 1. Because the Rogowski coil has the advantage of higher linearity compared to the CT, the loop gain is easier to control. Therefore, it is more suitable to design an FF-CSCI type AEF based on the Rogowski CM current sensor.

The CM equivalent circuit of the FF-CSCI AEF is shown in Fig. 11. The current of AEF can be expressed as

$$I_{AEF} = \frac{I_{LISN}Z_{LISN} - (I_{LISN} + I_{AEF})G_{FF}}{Z_{\text{inj}}} \tag{27}$$

where Z_{inj} is the injection impedance of the AEF, G_{FF} is the feedforward gain of the AEF, and Z_{LISN} is the LISN impedance. The equivalent impedance Z_{AEF} of the AEF can be expressed as

$$Z_{AEF} = \frac{I_{LISN}}{I_{AEF}}Z_{LISN} = \frac{Z_{\text{inj}} - G_{FF}}{Z_{LISN} - G_{FF}}Z_{LISN}. \tag{28}$$

When $Z_{\text{inj}} = G_{\text{FF}}$, the equivalent impedance of the AEF falls to 0, independent of the LISN impedance. Therefore, the feedforward gain G_{FF} of the AEF should be as close as possible to Z_{inj} within the concerned frequencies so that the Z_{AEF} is as small as possible.

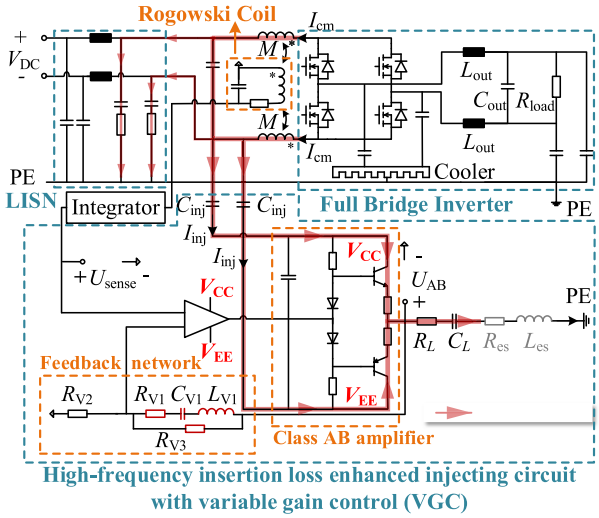

Fig. 12 Schematic diagram of the total AEF.

However, the complexity of the injection impedance is increased by the influence of the parasitic parameters of the actual circuit. Therefore, in this work, a closed-loop variable gain control (VGN) method is proposed to enhance high-frequency performance. The principle and design process are as follows.

B. High-Frequency Insertion Loss Enhanced Design

The schematic diagram and connection of the high-frequency insertion loss enhanced injecting circuit with variable gain control (VGC) are shown in Fig. 12, which consists of a class AB amplifier, a feedback network, an op-amp, injecting capacitors C_{inj}, load capacitor C_{L} and load resistor R_{L}. To accurately calculate the required forward gain G_{FF} of the AEF, the parasitic resistance R_{es} and parasitic inductance L_{es} in the injecting branch are also considered (shown in gray).

The class AB amplifier enhances the output current capability of the op-amp while the feedback network controls the output of the class AB amplifier. R_{V3} is used to suppress the low-frequency gain and LC resonant of the circuit, which can be ignored when analyzing.

The mapping of the component in Fig. 11 to those in Fig. 12 is

$$\begin{cases} Z_{\text{inj}} = 2/(sC_{\text{inj}}) + R_{es} + 1/(sC_L) + R_L + sL_{es} \\ G_{FF} = [R_{V1} + 1/(sC_{V1}) + sL_{V1}]/R_{V2} \end{cases}. \tag{29}$$

According to the analysis of Section A, reasonable circuit parameters should be set to realize $Z_{\text{inj}} = G_{\text{FF}}$. Therefore, the composition of Z_{inj} should be analyzed.

C_{L} and C_{inj} are equivalent to the Y-capacitors in the passive filter, and are typically several nanofarads to tens of nanofarads in value.

There are two main sources of R_{es}. One is the equivalent parasitic resistance of the capacitor C_{Y} and C_{inj}. Fig. 13 shows the impedance Z_{C} and capacitive reactance X_{C} curves for 3

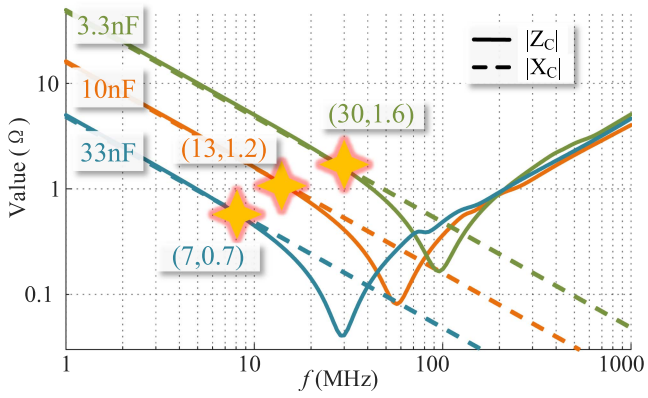

Fig. 13. Z_C and X_C of different capacitors.

capacitors of different values produced by Murata. When the capacitance is larger than 3.3nF, the equivalent series resistance ESR can't be ignored within 30 MHz. Another source is the op-amp. At high frequencies, the class AB amplifier has limited current amplification capability while the closed-loop output impedance of the op-amp rises, which is equivalent to the increase of R_{es}.

Therefore, R_L is added to mitigate the variation of R_{es} within the concerned frequencies.

L_{es} comes from the parasitic inductance of the ground lead. Usually, the PE of the AEF needs to be connected to the chassis of the interfering equipment through a lead. The parasitic inductance of the lead can be calculated by an empirical formula

$$L_{lead} = 2l_{lead} \cdot [\ln(2l_{lead}/r_{lead}) - 0.75] \cdot 10^{-7} \quad (30)$$

where l_{lead} and r_{lead} are the length and the radius of the lead, respectively. For a 20 mm×1.5 mm^2 lead, L_{lead} is calculated to be 13 nH, suggesting an impedance of 2.5Ω at 30 MHz. Therefore, the impact of the lead cannot be ignored.

Based on the above analysis, it is evident that the parasitic parameters influence Z_{inj} significantly. To minimize this effect, the feedforward gain G_{FF} must vary with frequency. That is to say, the feedback network should have different feedback coefficients at different frequencies, which can be realized by the following steps.

1) Estimate L_{es} and R_{es} values according to (30) and datasheets of op-amp and transistor respectively.
2) Set R_L as several times of R_{es}.
3) Set the component values of the feedback network (shown in Fig. 12) in the injecting circuit according to (29) so that G_{FF} is close to Z_{inj}.

Similar to the LCN proposed in Section II, the VGC method only introduces additional passive components, so the cost increment is limited.

To verify the performance of variable gain control (VGC), a stability analysis is carried out first. The transfer function diagram of the total VGC loop is shown in Fig. 14, where Z_{inj} has been derived and G_F equals to G_{FF} in (29). $G_{AB.L}$ is defined as $G_{AB.L} = Z_{inj}/(Z_{AB} + Z_{inj})$. G_{op}, G_{AB0} and Z_{AB} are the open-loop gain of the op-amp, the empty-load gain of the class AB amplifier, and the output impedance of the class AB amplifier, respectively. They can be derived from datasheets or by experimental measurement. Finally, the Bode plot of the open-loop transfer function of the VGC loop is figured out, as shown in Fig. 15.

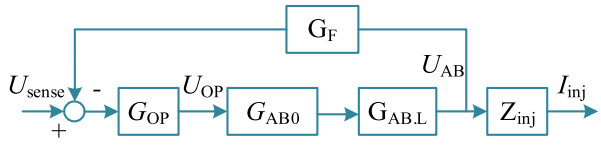

Fig. 14 Function block of the VGC loop.

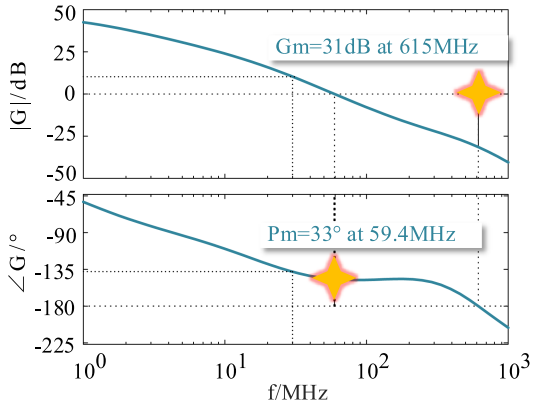

Fig. 15 Open-loop Bode diagram of the VGC loop.

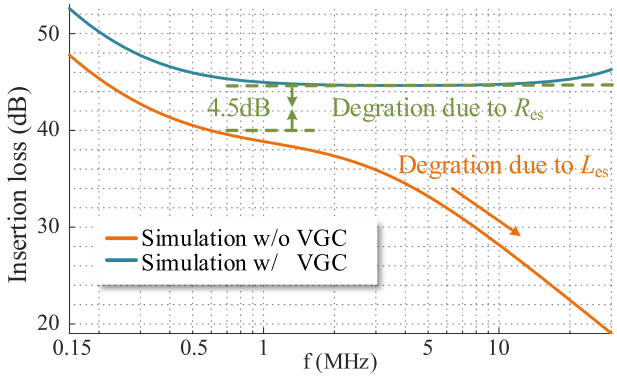

Fig. 16 Simulation of insertion loss with VGC and without VGC.

The result indicates a gain margin G_m of 31 dB and a phase margin P_m of 33°. Generally, a gain margin greater than 6 dB and a phase margin greater than 30° are considered stable [34]. The phase response stays at least 44° away from −180° from 150 kHz to 30 MHz, demonstrating robust disturbance rejection capability at the working frequency of the AEF.

Further, a simulation of the insertion loss is made. It is assumed that the sensing part works ideally. The variation of R_{es} with frequencies is ignored. Then set R_{es} is 0.1Ω and the length of the ground lead is 2 cm. With reference to the existing insertion loss simulation method [35], the internal resistance of the noise source is set to 50Ω.

The simulation result is shown in Fig. 16. As a comparison, the conventional method ignores all parasitic parameters when setting G_{FF}, so the gain control circuit degrades to an integrator

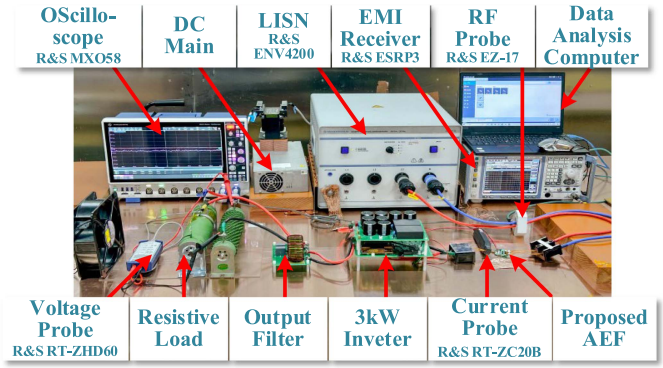

Fig. 17 Overall layout of AEF experimental platform.

TABLE II
MAIN PARAMETERS OF THE 3 KW INVERTER

Parameter	Symbol	Value
Input voltage	V_{in}	300 V
Input current	I_{in}	10 A
Output voltage	V_{out}	200 V
Output current	I_{out}	15 A
Output filtering inductance	L_{out}	300 μH
Output filtering capacitance	C_{out}	940 nF
Load Resistance	R_{load}	13.3 Ω
Switching frequency	f_{sw}	50 kHz

[22]. At the low frequencies, the insertion loss of the conventional method decreases by 4.5 dB due to not considering the voltage landings on R_{es}. At high frequencies, the insertion loss decreases linearly with frequency due to the increasing voltage drop on L_{es}. The simulation proves the necessity of the variable gain control.

IV. EXPERIMENT VERIFICATION

As shown in Fig. 17, a 3 kW inverter experimental platform is built to evaluate the performance of the proposed AEF. The main parameters of the inverter are shown in Table II. The main parameters of the AEF parts are shown in Table III. To compare the filtering performance, a passive filter (PEF) is also adopted, where the CM inductance L_{cm} is 503 μH and the Y-capacitor C_Y is 47nF. Both the PEF and AEF are designed to comply with the CISPR-11 EMI standard in order to make a fair comparison for the volumes. The sum of the Y-capacitance in the PEF is approximately equal to the value of the total equivalent capacitance in the injected part of the AEF, i.e., $2C_Y \approx (C_L//2C_{inj})$. The structure of the proposed AEF is shown in Fig. 18. The power line conductors of the inverter first pass through the sensing PCB on the bottom, and then reach the injecting PCB on the top. The dimensions of the AEF and the PEF are shown in Fig. 19. Thanks to the volume advantage of the Rogowski coil and the stacked-board design, the volume of the AEF decreases by 90%

TABLE III
MAIN PARAMETERS OF THE PROPOSED AEF

Part	Symbol	Value
Sensing part (Rogowski coil)	N	37
	l_1	3.6 mm
	l_2	10 mm
	h	1.6 mm
Sensing part (integrator with LCN)	R_N	120 Ω
	C_F	100 pF
	R_{c2}	270 Ω
	C_{c1}	390 pF
	C_{res}	100 pF
	L_{res}	180 nH
Injecting part (with VGC)	C_{inj}	100 nF
	C_L	200 nF
	R_L	1 Ω
	R_{v1}	100 Ω
	C_{v1}	1 nF
	L_{v1}	1.5 uH
	R_{v2}	100Ω

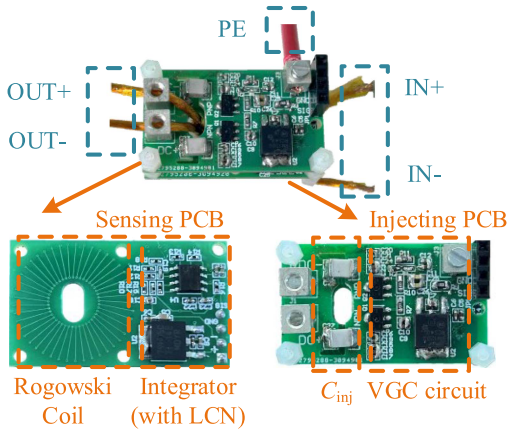

Fig. 18 Structure of the proposed AEF.

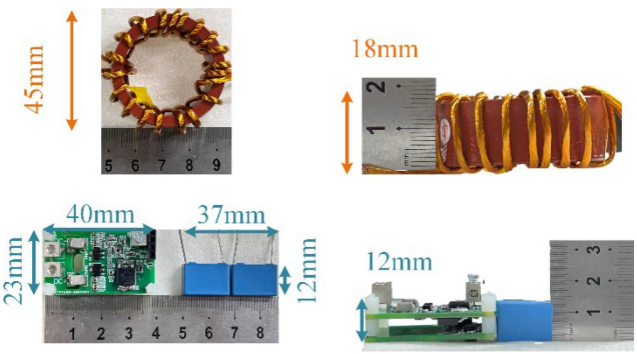

Fig. 19 Size comparison of the proposed AEF and PEF.

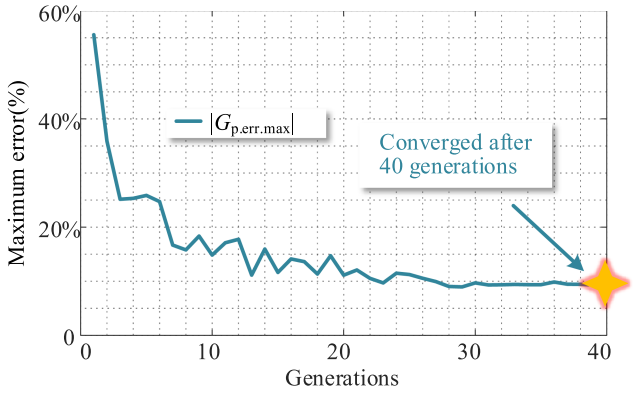

Fig. 20 The iterative curve of the LCN parameter optimization.

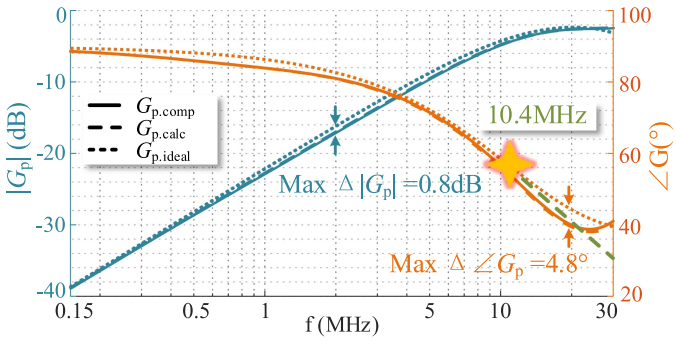

Fig. 21 Optimization result of the LCN parameters.

compared to that of the PEF. In addition, the size of the Rogowski coil is only $10 \times 10 \times 1.6$ mm, which is much smaller than CTs.

To verify the effectiveness of the high-order lead compensation network (LCN) in Section II, the injecting impedance Z_{inj}, the input of integrator $U_{\text{p.act}}$ and the output of the AEF $U_{\text{out.act}}$ are measured experimentally. Next, the optimization is performed according to Fig. 10. The iteration curves of the algorithm are shown in Fig. 20. By setting reasonable initial conditions, the algorithm converges rapidly after 40 generations. The optimization result is shown in Fig. 21. The algorithm shows that the phase of the ideal input of the op-amp $G_{\text{p.ideal}}$ (noted as $\angle G_{\text{p.ideal}}$) should increase at high frequencies, suggesting that there is a phase lag in the transform function of the AEF. The lead compensation needs to be added when the frequency is higher than about 10.4 MHz. After optimization, both the theoretical calculation value and actual value of G_{p} (noted as $G_{\text{p.calc}}$ and $G_{\text{p.comp}}$, respectively) are close to the ideal gain $G_{\text{p.ideal}}$. It should be noted that $G_{\text{p.comp}}$ and $G_{\text{p.calc}}$ are slightly different due to the restriction and deviation of the components, but the phase error between $G_{\text{p.comp}}$ and $G_{\text{p.ideal}}$ is still smaller than 4.8 degrees.

Then, to verify the performance of the proposed CM current sensor, the impedance curve of the coil is measured by impedance analyzer HIOKI IM7581, as shown in Fig. 22. The measurement result shows the resonant frequency of the coil is 101.55 MHz, suggesting a sufficient bandwidth to measure the CM current at 150 kHz–30 MHz.

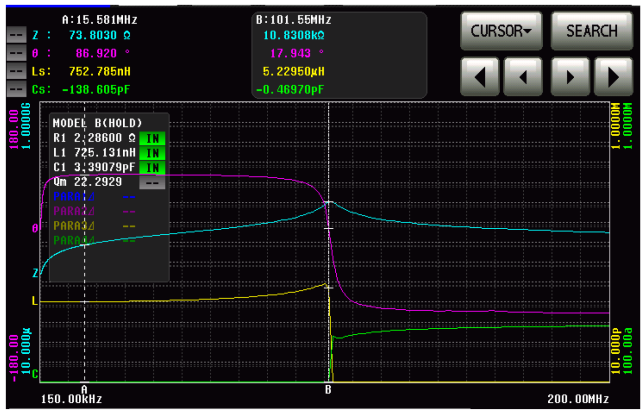

Fig. 22 Impedance curve of the coil measured by the impedance analyzer.

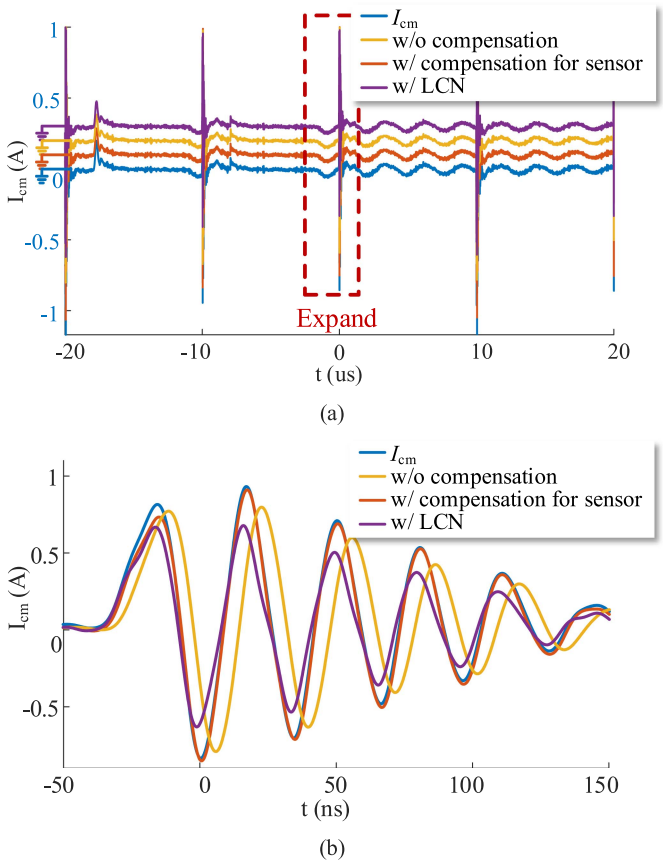

Fig. 23 Measured result of I_{cm} in time domain: (a) Overview and (b) detail.

Next, the CM current of the inverter is measured by the proposed Rogowski coil CM current sensor, and the results are compared with that of the current probe R&S RT-ZC20B with 100 MHz bandwidth. The results are shown in Fig. 23. As shown in Fig. 23(a), all groups performed well when measuring low-frequency current. However, as shown in Fig. 23(b), with signal frequencies approaching 30 MHz, the situation differs

1) Due to the output impedance increase and the resonant effect of the Rogowski coil, the uncompensated group shows phase lag and amplitude decrease.

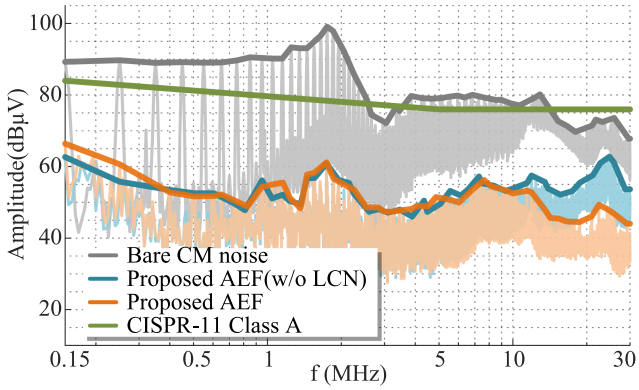

Fig. 24 Noise spectrum comparison of AEF with and without LCN.

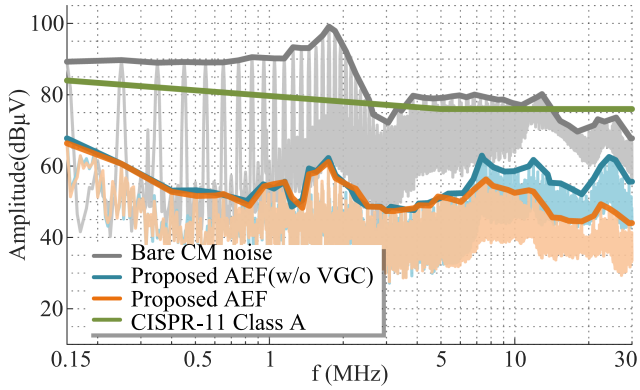

Fig. 25 Noise spectrum comparison of AEF with and without VGC.

2) By only compensating for the phase lag of the sensor, regardless of the injecting circuit, the measurement matches that of the current probe.
3) By using the proposed LCN which compensates for phase lag of both the sensor and the injecting circuit, the measurement result shows a phase lead. It indicates that there is an error in the sensor, but this happens to be the original purpose of the LCN design: to compensate for the error generated by the phase lag of the injection section by sacrificing the accuracy of the sensing part.

To further verify the compensation effect of LCN, as well as the effect of the VGC injecting method, four groups of experiments are performed.

With LCN VS without LCN: As shown in Fig. 24, with LCN, the insertion loss degradation caused by the phase lag in the injecting circuit is effectively mitigated. The amplitude of the CM current at 10 MHz–30 MHz is significantly reduced. The insertion loss with the LCN method is 22.8 dB–30.3 dB at 10 MHz–30 MHz, suggesting an improvement of 15 dB. Although compensation for the sensor error has been added in the w/o LCN group, the insertion loss still decreases at high frequencies. It proves the necessity for the proposed LCN to compensate for the phase lag of the injecting circuit. It should be noted that the LCN method relies on the simplicity and determinism of the equivalent circuit of the Rogowski coil. For CTs, the equivalent circuit is far more complex than that of the Rogowski coil due to the nonlinear and saturation characteristics of the magnetic core [36], [37]. Therefore, the lead compensation method cannot be applied to CTs.

With VGC VS without VGC: As shown in Fig. 25, compared with the traditional method without VGC, the amplitude of the CM current in the 7 MHz–30 MHz frequency is significantly reduced. The maximum insertion loss improvement is 14.2 dB. The variable gain control considers the parasitic parameters of the injecting part and adjusts the feedforward gain G_{FF} according to them, thus increasing the high-frequency insertion loss.

With AEF VS with PEF: As shown in Fig. 26, at 150 kHz–2 MHz, the impedance of the Y-capacitors in conventional PEF is too large to bypass for the CM current. In contrast, the proposed AEF reaches the maximum insertion loss of 44.7 dB at 1.4 MHz

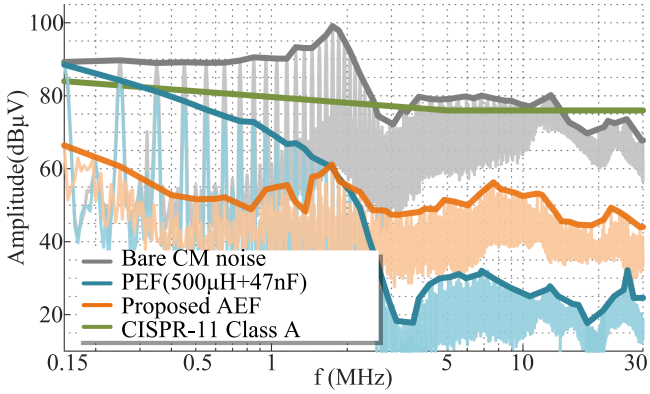

Fig. 26 Noise spectrum comparison of AEF and PEF.

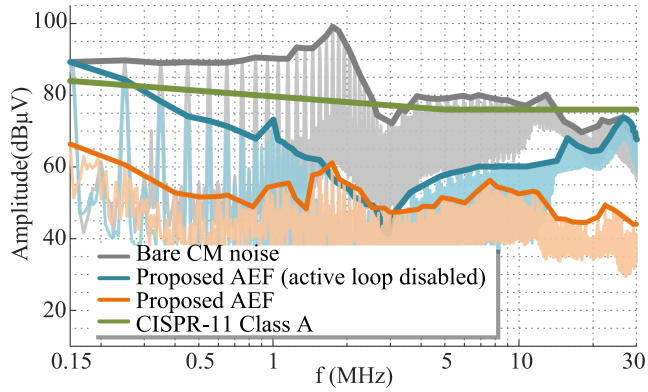

Fig. 27 Noise spectrum comparison of AEF with and without active loop enabled.

and brings an insertion loss improvement up to 27 dB. Although the PEF has a larger insertion loss than the proposed AEF at 2 MHz–30 MHz, the proposed AEF already has a larger insertion loss margin. Affected by the limited low-frequency filtering performance, the PEF still needs to increase the CM inductance to keep the noise below the limit line. In other words, the proposed AEF has a more balanced insertion loss in the whole concerned frequency band, thus reducing the size.

With AEF (active loop enabled) VS with AEF (active loop disabled): As shown in Fig. 27, at 150 kHz–1.5 MHz, the insertion loss of the active loop disabled group is significantly less

than that of the enabled group, because the voltage drop across the Y-capacitors cannot be canceled, so the branch impedance is large at low frequencies. At 1.5 MHz–3 MHz, the insertion loss of the disabled group is comparable to that of the enabled group. However, when the frequency reaches 3 MHz–30 MHz, due to the resonance effect of the Y-capacitor, the insertion loss of the disabled group is again lower than that of the enabled group. The experimental result demonstrates the effectiveness of the active loop design.

V. Conclusion

In this article, a high-frequency insertion loss enhanced AEF based on a Rogowski coil is proposed. The Rogowski coil replaces the CT, resulting in a significant reduction in the size of the sensing part. Experiments show that the VGC method and the LCN improve the insertion loss at high frequencies. With a small size of 38 mm $\times$ 23 mm, the proposed AEF achieves an insertion loss of 22.8 dB–30.3 dB at 10 MHz–30 MHz and a maximum of 44.7 dB at 1.4 MHz.

References

[1] S. Wei, Z. Zhao, L. Yuan, W. Wen, and K. Chen, "Voltage oscillation suppression for the high-frequency bus in modular-multiactive-bridge converter," *IEEE Trans. Power Electron.*, vol. 36, no. 9, pp. 9737–9742, Sep. 2021.

[2] J. Biela, A. Wirthmueller, R. Waespe, M. L. Heldwein, K. Raggl, and J. W. Kolar, "Passive and active hybrid integrated EMI filters," *IEEE Trans. Power Electron.*, vol. 24, no. 5, pp. 1340–1349, May 2009.

[3] H. Peng, B. Narayanasamy, A. I. Emon, Z. Yuan, M. U. Hassan, and F. Luo, "Design and implementation of selective active EMI filter with digital resonant controller," in *Proc. 2020 IEEE Energy Convers. Congr. Expo.*, 2020, pp. 5855–5861.

[4] Y. Sha, W. Chen, Z. Zhao, F. Zhang, C. Pei, and Z. Chen, "Research of active EMI suppression strategy for high power density power supply," in *Proc. 2018 IEEE Appl. Power Electron. Conf. Expo.*, 2018, pp. 611–614.

[5] "How active EMI filter ICs mitigate common-mode emissions and increase power density in single- and Three-phase power systems," Texas Instruments, Mar. 2023. [Online]. Available: https://www.ti.com/lit/wp/slvafj9/slvafj9.pdf

[6] H. Li, S. Wang, C. Zhang, and Z. Wang, "A Compact passive-active hybrid EMI filter with phase compensation for power converters," in *Proc. 2022 4th Int. Conf. Smart Power Internet Energy Syst.*, Beijing, China, 2022, pp. 510–516.

[7] Y. Zhou et al., "A novel virtual capacitance enhancement-based active EMI filter for CM noise attenuation," *IEEE Trans. Ind. Electron.*, vol. 71, no. 12, pp. 16870–16874, Dec. 2024.

[8] D. Shin, S. Jeong, Y. Baek, C. Park, G. Park, and J. Kim, "A balanced feedforward current-sense current-compensation active EMI filter for common-mode noise reduction," *IEEE Trans. Electromagn. Compat.*, vol. 62, no. 2, pp. 386–397, Apr. 2020.

[9] D. Shin, S. Jeong, and J. Kim, "Quantified design guidelines of a compact transformerless active EMI filter for performance, stability, and high voltage immunity," *IEEE Trans. Power Electron.*, vol. 33, no. 8, pp. 6723–6737, Aug. 2018.

[10] H. Li, S. Wang, C. Zhang, and B. Zhang, "Dual-current-injection CSCC active common-mode EMI filters with high insertion loss for DC-DC converters," *Chin. J. Elect. Eng.*, vol. 8, no. 4, pp. 19–29, Dec. 2022.

[11] W. Chen, X. Yang, and Z. Wang, "Analysis of insertion loss and impedance compatibility of hybrid EMI filter based on equivalent circuit model," *IEEE Trans. Ind. Electron.*, vol. 54, no. 4, pp. 2057–2064, Aug. 2004.

[12] Z. Darning and K. J. Tseng, "Effect of high permittivity and core dimensions on the permeability measurement for Mn-Zn ferrite cores used in high-frequency transformer," in *Proc. 3rd IEEE Int. Workshop Electron. Des., Test Appl.*, Kuala Lumpur, Malaysia, 2006, pp. 6, Art. no. 378.

[13] M. Fritsch and M. Wolter, "High-frequency current transformer design and construction guide," *IEEE Trans. Instrum. Meas.*, vol. 71, 2022, Art. no. 9004309.

[14] A. N. Sarwade, P. K. Katti, and J. G. Ghodekar, "Use of Rogowski Coil for accurate measurement of secondary current contaminated with CT saturation in distance protection scheme," in *Proc. 2016 IEEE 6th Int. Conf. Power Syst.*, New Delhi, India, 2016, pp. 1–6.

[15] M. Zhu, D. J. Perreault, V. Caliskan, T. C. Neugebauer, S. Guttowski, and J. G. Kassakian, "Design and evaluation of Feedforward Active ripple filters," *IEEE Trans. Power Electron.*, vol. 20, no. 2, pp. 276–285, Mar. 2005.

[16] P. C. Saroj et al., "Development and Calibration of Rogowski coils for pulsed power systems," in *Proc. 2011 IEEE Int. Vac. Electron. Conf.*, Bangalore, India, 2011, pp. 471–472.

[17] L. Ming, Z. Xin, C. Yin, M. Chen, and P. C. Loh, "Integrator design of the rogowski current sensor for detecting fast switch current of SiC devices," in *Proc. 2019 IEEE Energy Convers. Congr. Expo.*, Baltimore, MD, USA, 2019, pp. 4551–4557.

[18] S. Jeong, D. Shin, J. Kim, J. Kim, and S. Kim, "Design of effective surge protection circuits for an active EMI filter," in *Proc. 2017 Asia-Pacific Int. Symp. Electromagn. Compat.*, Seoul, Korea (South), 2017, pp. 210–212.

[19] L. Dai, W. Chen, X. Yang, M. Zheng, Y. Yang, and R. Wang, "A multifunction common mode choke based on active CM EMI filters for AC/DC power converters," *IEEE Access*, vol. 7, pp. 43534–43546, 2019.

[20] Y. Zhang, Q. Li, and D. Jiang, "A motor CM impedance based transformerless active EMI filter for DC-Side common-mode EMI suppression in motor drive system," *IEEE Trans. Power Electron.*, vol. 35, no. 10, pp. 10238–10248, Oct. 2020.

[21] S. Jiang, Y. Liu, W. Liang, J. Peng, and H. Jiang, "Active EMI filter design with a modified LCL-LC filter for single-phase grid-connected inverter in vehicle-to-grid application," *IEEE Trans. Veh. Technol.*, vol. 68, no. 11, pp. 10639–10650, Nov. 2019.

[22] Z. Zhang and A. M. Bazzi, "A virtual impedance enhancement based transformer-less active EMI filter for conducted EMI suppression in power converters," *IEEE Trans. Power Electron.*, vol. 37, no. 10, pp. 11962–11973, Oct. 2022.

[23] S. Tolle, D. Kübrich, and S. Frei, "An active EMI filter for robust integration in medium and high-power AC/DC converters," *IEEE Trans. Electromagn. Compat.*, vol. 66, no. 6, pp. 1769–1779, Dec. 2024.

[24] Q. Chen, P. Zhou, X. Pei, and Z. Zhang, "Modeling, evaluation, and optimization of active common-mode EMI filter based on phasor analysis," in *Proc. 2024 IEEE 7th Int. Elect. Energy Conf.*, Harbin, China, 2024, pp. 3331–3338.

[25] L. A. Kojovic, "Split-core PCB Rogowski coil designs and applications for protective relaying," in *Proc. 2003 IEEE PES Transmiss. Distrib. Conf. Expo. (IEEE Cat. No.03CH37495)*, Dallas, TX, USA, 2003, vol. 1, pp. 269–273, doi: 10.1109/TDC.2003.1335233.

[26] S. Fu et al., "Current measurement method of multiple chips using rectangular PCB rogowski coils integrated in press pack IGBT device," *IEEE Trans. Power Electron.*, vol. 38, no. 1, pp. 96–100, Jan. 2023, doi: 10.1109/TPEL.2022.3205353.

[27] J. Wang, S. Li, X. Yu, R. Zhou, Z. Zhu, and W. Chen, "Analysis of influencing factors on current measurement accuracy of PCB Rogowski coil," *IEEE Sensors J.*, vol. 25, no. 6, pp. 9531–9539, Mar. 2025.

[28] Z. Xin, Y. Yao, J. Kang, Q. Li, Z. Zhou, and Y. Shi, "A closed-loop compensated Rogowski coil current sensor for three-phase inverter," *IEEE Trans. Power Electron.*, vol. 40, no. 1, pp. 2126–2138, Jan. 2025, doi: 10.1109/TPEL.2024.3464121.

[29] Y. Shi, Z. Xin, Z. Zhou, and Y. Yao, "Design and modeling of the PCB Rogowski coil with multiple vias for power devices," in *Proc. 2023 IEEE 2nd Int. Power Electron. Application Symp.*, Guangzhou, China, 2023, pp. 1072–1076.

[30] Y. Zhang and D. Jiang, "An active EMI filter in grounding circuit for DC Side CM EMI suppression in motor drive system," *IEEE Trans. Power Electron.*, vol. 37, no. 3, pp. 2983–2992, Mar. 2022.

[31] J. N. Fritz, C. Neeb, and R. W. De Doncker, "A PCB integrated differential Rogowski coil for non-intrusive current measurement featuring high bandwidth and dv/dt immunity," in *Proc. Power Energy Student Summit*, 2015, pp. 1–6.

[32] J. Gong et al., "Overcurrent Protection Enabled by Broadband Rogowski Coil Current Sensor for Medium-voltage SiC MOSFET," *IEEE Trans. Power Electron.*, vol. 40, no. 5, pp. 6847–6859, May 2025.

[33] H. R. E. H. Bouchekara, "Electric charged particles optimization and its application to the optimal design of a circular antenna array," *Artif. Intell. Rev.*, vol. 54, no. 3, pp. 1767–1802, 2021.

[34] P. R. Gray, P. J. Hurst, S. H. Lewis, and R. G. Meyer, *Analysis and Design of Analog Integrated Circuits*, 5th ed. New York, NY, USA: Wiley, 2009.

[35] L. Dai, W. Chen, X. Yang, M. Zheng, Y. Yang, and R. Wang, "A multifunction common-mode choke based on active CM EMI filters for AC/DC power converters," *IEEE Access*, vol. 7, pp. 43534–43546, 2019.
[36] F. Baig et al., "Comparative analysis of various magnetic cores for current sensing in active EMI filters," in *Proc. 2024 Int. Symp. Electromagn. Compat. – EMC Europe*, 2024, pp. 1003–1008.
[37] N. Kondrath and M. K. Kazimierczuk, "Bandwidth of current transformers," *IEEE Trans. Instrum. Meas.*, vol. 58, no. 6, pp. 2008–2016, Jun. 2009.

Yuan Feng (Student Member, IEEE) was born in Guangdong, China, in 1998. He received the B.S. degree in electrical engineering from the Changsha University of Science & Technology, Changsha, China, in 2021. He is currently working toward the Ph.D. degree in electrical engineering with Hunan University, Changsha, China.

His research interests include electromagnetic sensing, electromagnetic compatibility, and capacitor condition monitoring.

Peng Guo (Member, IEEE) was born in Hunan, China, in 1992. He received the B.S. degree in electrical engineering from the Wuhan University of Technology, Wuhan, China, in 2015, and the Ph.D. degree in electrical engineering from Hunan University, Changsha, China, in 2020.

He is currently an Associate Professor with the College of Electrical and Information Engineering, Hunan University. His research interests include switch-mode power amplifier, data-driven nonlinear control, electromagnetic sensing, and electromagnetic compatibility for high-frequency power electronics systems.

Qianming Xu (Member, IEEE) was born in Henan, China, in 1989. He received the B.S. degree in electrical engineering and automation and the Ph.D. degree in electrical engineering from Hunan University, Changsha, China, in 2012 and 2017, respectively.

Since 2023, he has been a Professor with the College of Electrical and Information Engineering, Hunan University. His research interests include multilevel converter, power electronic reliability monitoring, and power quality control.

Cheng Tang was born in Hunan, China, in 1996. He received the B.S. degree in electrical engineering and automation and the Ph.D. degree in electrical engineering from Hunan University, Changsha, China, in 2019 and 2024, respectively.

He is currently a Postdoctoral Fellow with the College of Electrical and Information Engineering, Hunan University. His research interests include power conversion control, active thermal control, and model predictive control.

Yuanfa Peng was born in Henan, China, in 2002. He received the B.S. degree in electrical engineering, in 2024, from the Hunan University, Changsha, China, where he is currently working toward the M.S. degree in electrical engineering.

His research interests include an electromagnetic sensor, multiobjective optimization, and active EMI filter.

Qiaopo Xiong was born in Jiangxi, China, in 1988. He received the B.S. degree in electrical engineering from Central South University, Changsha, China, in 2009, and the Ph.D. degree in electrical engineering from Hunan University, Changsha, in 2014.

He is currently a Research Fellow with the Wuhan Maritime Communication Research Institute, Wuhan, China. His research interests include low frequency communication system and high-power electromagnetic transmitting technology and equipment.

Yandong Chen (Senior Member, IEEE) was born in Hunan, China, in 1979. He received the B.S. and M.S. degrees in instrument science and technology and the Ph.D. degree in electrical engineering from Hunan University, Changsha, China, in 2003, 2006, and 2014, respectively.

He was a Professor with the College of Electrical and Information Engineering, Hunan University. His research interests include power electronics for microgrid, distributed generation, power quality, and energy storage.

Dr. Chen is a recipient of the 2014 National Technological Invention Awards of China, and the 2014 WIPO-SIPO Award for Chinese Outstanding Patented Invention. He is a member of IEEE Power Electronics Society.

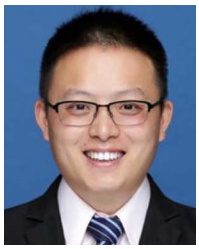

Zhikang Shuai (Senior Member, IEEE) received the B.S. and Ph.D. degrees in electrical engineering from the College of Electrical and Information Engineering, Hunan University, Changsha, China, in 2005 and 2011, respectively.

From 2009 to 2012, he was with Hunan University, as an Assistant Professor, an Associate Professor in 2013, and a Professor in 2014. His research interests include power quality control, power electronics, and microgrid stability analysis and control.

Dr. Shuai was the recipient of the 2010 National Scientific and Technological Awards of China, the 2012 Hunan Technological Invention Awards of China, and the 2007 Scientific and Technological Awards from the National Mechanical Industry Association of China. He is currently an Associate Editor for *CSEE Journal of Power and Energy Systems* and *Chinese Journal of Electrical Engineering*.

An Luo (Senior Member, IEEE) was born in Changsha, China, in 1957. He received the B.S. and M.S. degrees in industrial automation from Hunan University, Changsha, in 1982 and 1986, respectively, and the Ph.D. degree in fluid power transmission and control from Zhejiang University, Hangzhou, China, in 1993.

From 1996 and 2002, he was a Professor with the Central South University, Changsha. Since 2003, he has been a Professor with the College of Electrical and Information Engineering, Hunan University, where he is also the Chief of the National Engineering Research Center for Power Conversion and Control and the State Key Laboratory of High-Efficiency and High-Quality Conversion for Electric Power. His research interests include distributed generation, microgrid, and power quality.

Dr. Luo was the recipient of the highly prestigious China National Science and Technology Awards three times (2014, 2010, and 2006). He was elected to the Chinese National Academy of Engineering in 2015, the highest honor for scientists and engineers and scientists in China.